Deconvoluting the benefits of porosity distribution in layered electrodes on the electrochemical performance of Li-ion batteries

Abbos Shodiev, Mehdi Chouchane, Miran Gaberscek, Oier Arcelus, Jiahui Xu, Hassan Oularbi, Jia Yu, Jianlin Li, Mathieu Morcrette, Alejandro A. Franco

Energy Storage Materials 47 (2022) 462–471

Contents lists available at ScienceDirect

Energy Storage Materials

journal homepage: www.elsevier.com/locate/ensm

Deconvoluting the benefits of porosity distribution in layered electrodes on the electrochemical performance of Li-ion batteries

Abbos Shodiev[a,b], Mehdi Chouchane[a,b], Miran Gaberscek[e], Oier Arcelus[a,b], Jiahui Xu[a,b], Hassan Oularbi[a,b], Jia Yu[a,b], Jianlin Li[c], Mathieu Morcrette[a,b,d], Alejandro A. Franco[a,b,d,f,*]

[a] Laboratoire de Réactivité et Chimie des Solides (LRCS), UMR CNRS 7314, Université de Picardie Jules Verne, Hub de l'Energie, 15 rue Baudelocque, 80039 Amiens Cedex, France
[b] Réseau sur le Stockage Electrochimique de l'Energie (RS2E), FR CNRS 3459, Hub de l'Energie, 15 rue Baudelocque, 80039 Amiens Cedex, France
[c] Electrification and Energy Infrastructures Division, Oak Ridge National Laboratory, Oak Ridge, TN, 37831 United States
[d] ALISTORE-European Research Institute, FR CNRS 3104, Hub de l'Energie, 15 rue Baudelocque, 80039 Amiens Cedex, France
[e] Department of Materials Chemistry, National Institute of Chemistry, Hajdrihova 19, 1000 Ljubljana, Slovenia
[f] Institut Universitaire de France, 103 Boulevard Saint Michel, 75005 Paris, France

ARTICLE INFO

Keywords:
Lithium-ion batteries
Electrode heterogeneity
4D-resolved physical modeling
Ionic resistance
Symmetric cells

ABSTRACT

Thick Lithium Ion Battery (LIB) electrodes suffer from poor rate capability and high ionic impedance due to their thickness and mesostructure. Therefore, optimizing thick electrode architectures becomes crucial. In this work, we report a systematic assessment of the ionic resistance in heterogeneous porous electrodes through the combination of computational simulations using a 4D-resolved model and experimental measurements. The first part of the study is devoted to a general assessment of Electrochemical Impedance Spectroscopy (EIS) spectra, mapping the impact of ionic and electronic resistances on the overall impedances of uncalendered and calendered $LiNi_{1/3}Mn_{1/3}Co_{1/3}O_2$, $LiFePO_4$ and graphite electrodes. In the second part, *in silico*-generated electrodes with different porosities are used in computational EIS simulations to analyze the impact of the electrode porosity on the ionic impedance. As expected, the results show that a lower porosity leads to a higher ionic impedance because of a higher electrode tortuosity factor. Furthermore, *in silico*-generated electrodes with different porosities were stacked and assembled to create heterogeneities of porosity along the thickness, and used in computational EIS and galvanostatic discharge simulations. The computational results show that the porosity heterogeneity along the electrode thickness has a significant effect on the ionic impedance and capacity of the electrode. The electrode architecture with progressively decreasing porosity from separator to current collector shows the highest performance, a trend validated by our *in house* experimental EIS and galvanostatic discharge also reported in this manuscript. Overall, we conclude that the ionic resistance in a thick electrode can be effectively reduced through proper tuning of the porosity heterogeneity. The proposed heterogeneous electrode architectures presented here could enormously help building efficient thick electrodes for LIBs.

1. Introduction

Developing optimized energy conversion and storage devices has led to an unprecedented growth of the sustainable energy industry during the last three decades. Particularly, lithium-ion batteries (LIBs) have enabled consumer electronic technologies as well as the renaissance of the electric vehicles (EVs), due to their high energy and power densities, and long cycling stability [1]. Nevertheless, continuous improvements such as increasing energy density and decreasing manufacturing costs are still required to unlock their full potential [2,3]. State-of-the-art LIB chemistries are well engineered and can be designed for fast charging, yet electrodes need to be relatively thin leading to low energy densities and high costs [4]. Increasing electrode thickness and mass loading is a common approach to enhance the LIB energy density [3,5,6]. However, even if the lithium ion migration in a liquid electrolyte is several orders of magnitude higher than lithium diffusion in the solid phase, it is still the rate-limiting factor in a thick electrode and for electrodes under high C-rates [7,8]. Additionally, thick electrodes might also suffer from poor electrode wetting and dysfunctional heterogeneity in the electrode mesostructure [9,10]. These variations may lead to heterogeneous current distributions, increased ionic impedance, and fast electrolyte decomposition under high storage temperatures [11,12], resulting in lower energy and power capacities with accelerated cell degradation [13,14]. Therefore, optimizing thick electrode architectures becomes crucial for

* Corresponding author.
E-mail address: alejandro.franco@u-picardie.fr (A.A. Franco).

https://doi.org/10.1016/j.ensm.2022.01.058
Received 29 September 2021; Received in revised form 10 January 2022; Accepted 30 January 2022
Available online 1 February 2022

overcoming the limitations of electronic and ionic current distributions in LIBs [15].

Some experimental works have recently reported the interplay between energy and power density and electrode properties, such as areal loadings, porosities, and electrode architectures [7,8]. However, some electrode properties are challenging to engineer due to time, costs and instrument limitations [16]. In this regard, physical modeling serves as an efficient tool to address the electrochemical performance of LIBs, where optimization processes based on experimental trial and error become expensive and cumbersome [17]. For instance, several modeling studies were recently reported to quantify and address the heterogeneity issue at the single active material (AM) particle and the full electrode levels [18,19]. These models were built to describe how electrode heterogeneities affected its performance [18,19]. Furthermore, the ion migration limitation in the electrolyte phase of a porous electrode determines the LIB cell performance under high C-rate operation, an aspect which was independently and systematically studied in several works [7,8,20].

Electrochemical impedance spectroscopy (EIS) is one of the dominant tools to measure ionic resistance in the battery field [21]. The experimental setup to measure the ionic resistance of porous electrodes was first proposed by Ogihara *et al.* using a symmetric cell configuration [21]. Additionally, EIS constitutes a simple way to calculate the electrode tortuosity factor. Several authors already used symmetric cell configurations to measure the tortuosity factors of a graphite anode, a LFP cathode, and a NMC cathode [21–24]. Moreover, in a recent publication, we have reported for the first time a 4D (3D in space + time) physical model of a NMC electrode symmetric cell, which captures the impact of the spatial location of the AM and the carbon-binder domain (CBD) on the EIS response [25]. Our model allows assigning different physics to NMC, CBD and pores, and considers explicitly the electrochemical double layers at the NMC/electrolyte and CBD/electrolyte interfaces, which sets up a powerful ground for the characterization of ionic resistances in heterogeneous porous electrodes.

The present work aims at investigating the electrochemical response of electrodes with different porosity configurations. We particularly aim at assisting the design of thick electrodes with reduced ionic resistance and improved charge and discharge rate capabilities for LIBs. For this, we systematically investigate the ionic resistances of single layer and multi-layer electrodes with heterogeneous porosities along the thickness, to unravel possible guidelines of improvement of power densities of thick electrodes. After introducing the dual modeling-experimental methodology on which our study is supported, we discuss, based on our experimental data, ionic and electronic resistances contributions to the overall EIS for different electrode chemistries. Such data is used to calibrate our 4D-resolved model. The latter is employed to assess the EIS and discharge performance of *in silico*-generated electrodes with heterogeneous porosities along the electrode thickness. Electrodes are analyzed in terms of their tortuosity factors, and validation experiments are also reported. We finally conclude and indicate further directions for this work.

2. Methodology

2.1. Electrode structures generation

We have reported in our previous articles computational methods for stochastic and manufacturing simulation-based generation of LIB electrodes [26,27]. In this work, the stochastic method of electrodes generation was chosen to have electrodes with controlled porosity and keeping all the other parameters (*e.g.* electrode formulation) constant. The details of the technique can be found in Ref. [28] The obtained electrode mesostructures are meshed by using our voxelization algorithm INNOV in the Matlab® environment [29].

2.2. Pore size distribution

The pore phase of the generated electrodes was further segmented into individual pores using the watershed method to obtain pore size distribution of the studied mesostructures [9,10]. Specifically, the PoroDict library was used as part of the GeoDict® software package. Due to the discrete voxelated nature of the studied mesostructures, over-segmentation of the pore space is a common artifact induced by watershed-based methods. Many post-processing methods exist to alleviate the effect of such artifacts. In GeoDict® this is solved by reconnecting the initially segmented pores only if the percentage of surface area that is shared between them is bigger than a chosen value. A low threshold value results in many pores being reconnected, while the contrary happens when a high threshold value is selected. In this work, an intermediate value is carefully selected so that non-physical artifacts are eliminated. Once the pore space is labeled, the diameters of equivalent volume spheres are calculated and arranged in a histogram. The histogram is further normalized to account for the non-uniform selection of the number of histogram bins.

2.3. EIS model and simulation procedure

The imported volumetric multi-phase mesh consists of five subdomains: active material (AM) and carbon binder domain (CBD) particles, separator (coming from computer tomography-acquired imaging), current collectors, and electrolyte [30]. The equations behind the 3D EIS model and geometry subdomains are provided in one of our previous publications [25]. The EIS spectra were calculated in Comsol Multiphysics 5.4 environment using the Battery Module. The impedance was calculated at seven frequencies per decade, ranging from 1 to 10^7 Hz with 10 mV perturbation. The simulations were performed using a computer equipped with an Intel® Xeon® E5–4627 Cache @ 3.30 GHz with 264 GB of RAM. Each simulation took approximately 15 to 30 hours, depending on the input parameters (electronic conductivity of active material) and the electrode mesostructure.

2.4. Electrode tortuosity factor calculations

Electrode tortuosity factor (τ_{EIS}) values were calculated from the EIS data generated by the computer simulations by using the graphical method proposed by Landesfeind *et al.* [24] based on the following expression:

$$\tau_{EIS} = \frac{R_{ion} A \varepsilon k}{2d} \tag{1}$$

where R_{ion} is the ionic resistance within the electrode extracted from impedance data, A is the surface area of the electrode, ε is the electrode porosity, k is the bulk ionic conductivity of the electrolyte and d is the thickness of the electrode [24].

The direct assessment of the tortuosity factors (τ_{factor}) of the computer-generated electrode mesostructures was performed by using the TauFactor software in the Matlab® environment [31]. This software solves Fickean diffusion equations in steady-state after application of a concentration difference between two opposing faces in the electrode along its thickness. The tortuosity factor τ_{factor} is given in this case by:

$$\tau_{factor} = \frac{D}{D_{eff}} \varepsilon \tag{2}$$

with D being the bulk diffusion coeffient and D_{eff} the effective diffusion coefficient.

2.5. Discharge model and simulation procedure

Once the meshed electrode mesostructure is imported into COMSOL Multiphysics, an electrochemical model was applied to simulate a single discharge at 3C starting from a fully charged battery cell. The model is

Table 1
List of analyzed experimental electrodes.

Name	Active material (dry mass%)	Carbon black (dry mass%)	Binder (dry mass%)	Porosity (%)	Thickness (μm)
Uncalendered-NMC-96	$LiNi_{1/3}Mn_{1/3}Co_{1/3}O_2$ (96%)	C65 (2%)	PVdF (2%)	49%	144
Calendered-NMC-96	$LiNi_{1/3}Mn_{1/3}Co_{1/3}O_2$ (96%)	C65 (2%)	PVdF (2%)	28%	73
Uncalendered-LFP-96	$LiFePO_4$ (96%)	C45 (2%)	PVdF (2%)	64%	122
Calendered-LFP-96	$LiFePO_4$ (96%)	C45 (2%)	PVdF (2%)	37%	64
Uncalendered-graphite-96	GHDR 10–4 (95%)	C45 (2%)	CMC/SBR (1.5%/1%)	56%	157
Calendered-graphite-96	GHDR 10–4 (95%)	C45 (2.5%)	CMC/SBR (1.5%/1%)	28%	95
Uncalendered- NMC-PVDF-HFP-C45	$LiNi_{1/3}Mn_{1/3}Co_{1/3}O_2$ (73%)	C45 (7%)	PVdF (20%)	55.6%	127
Calendered-NMC-PVDF-HFP-C45	$LiNi_{1/3}Mn_{1/3}Co_{1/3}O_2$ (72.7%)	C45 (19.5%)	PVdF-HFP (7.8%)	44%	85

identical to the one reported in some of our previous studies [26,30]. Each discharge simulation took between 5 and 9 h to complete on a desktop computer with 64 GB of RAM.

2.6. Experimental methodology

As-received materials were used including $LiNi_{1/3}Mn_{1/3}Co_{1/3}O_2$ (NMC, Umicore), $LiFePO_4$ (LFP, Aleees), C–NERGYTM super C65, C45 carbon black and GHDR 10–4 graphite (IMERYS), Solef^{TM} Polyvinylidene fluoride (PVdF, Solvay), Carboxymethyl Cellulose (CMC, ACROS Organics), Styrene-Butadiene Rubber (SBR, Zeon), Triton X-100 (TX, Sigma-Aldrich), N-methyl pyrrolidone (NMP, BASF), Tetrabutylammonium perchlorate ($TBAClO_4$, Alfa Aesar) and Poly (vinylidene fluoride-co-hexafluoropropylene) (PVdF-HFP, Kynar Flex2801, Arkema).

The NMC, LFP, and graphite electrodes that we used as control electrodes were prepared in the usual way. First, the solid components, including active material, carbon black, and binder, were premixed with a soft blender. Then, the solvent was added until the desired solid content (SC) was achieved. A Dispermat CV3-PLUS high-shear mixer was used for the slurry preparation. The NMC and LFP slurries were mixed for two hours, while the graphite slurries were mixed overnight, in a water-bath cooled recipient at 25 °C. The resulting NMC and LFP mixtures were then coated over a 22 μm thick aluminum current collector, and the graphite mixture was coated over a 18.6 μm thick copper current collector, using a comma-coater prototype-grade machine. For the electrodes with controlled porosity and the bi-porous electrodes, the Bellcore process was used [32]. The solid components were ground with an agate mortar and then moved to a glass container. Different volumes of dibutyl phthalate, calculated according to the volume ratio, were added as a porogen agent. Acetone was added as a solvent, and the mixture was well mixed with a magnetic stirrer at high speed. The slurry was then deposited on a Mylar foil by doctor blading. The films detached from the Mylar foil were dried in ambient temperature and combined to one electrode under 10 Pascal at 130 °C. The bi-porous electrode was then soaked 3 times in dimethyl-ether during 15 min in ether to remove the porogen agent. The analyzed electrodes in this work are listed in Table 1.

All EIS tests were performed in 2035-coin cells assembled in a dry room (H_2O < 15 ppm). The electrodes were punched and assembled into symmetric coin cells (both at the positive and negative side) using Celgard 2500 as separator (thickness = 25 μm, porosity = 55%). The electrolyte was a 10 mM $TBAClO_4$ solution, prepared in a 1:1 wt mixture of ethylene carbonate:dimethyl carbonate. The EIS was performed with a BioLogic MTZ-35 impedance analyzer, in the range of 10^{-1} – 10^6 Hz with a potential perturbation of 10 mV. All measurements were carried out at 25 ± 1 °C.

3. Results and discussion

3.1. Deconvoluting ionic resistance from EIS

It is frequent practice to represent the EIS response as Nyquist plots. The typical shape of a Nyquist plot for symmetric cells results from an about 45° slope line followed by an about 90° vertical line at low frequencies. The high-frequency intercept on the x-axis represents a pure resistor while the response at the lowest frequencies tends to a vertical line representing a purely capacitive behavior. Between these two frequency regions, slopes with 45° represent the resistance caused by ion migration inside the porous electrode [33,34]. Furthermore, sometimes a semicircle-shaped spectrum shows up in mid-high frequency intervals for some electrode materials. Since in symmetric cell experiments the blocking electrolyte ensures that no faradaic current flows during the EIS characterization, this arc-like EIS response cannot be related to a charge transfer process, as usually observed in LIB electrodes.

In the present symmetric cells, this semicircle is ascribed in the literature to several factors such as the contact electronic resistance at the current collector/composite electrode interface and bulk AM electronic conductivity [33]. The capacitive element can originate from the electrical double layer formation that occurs at the current collector/electrolyte interface (*i.e.* the electrolyte phase inside the pores of the composite that wets the current collector substrate)[34]. On top of that, the electronic conductivity of the AM generates a high frequency semicircle too. As Landesfeind *et al.* pointed out, if a high electronic conductivity condition is not met, both ionic and electronic effects will play a role in the total resistance measured by impedance, which hinders the measurement of pure ionic resistances [24,35].

Fig. 1 shows our experimentally obtained EIS plots for uncalendered and calendered NMC, LFP, and graphite electrodes in symmetric cell configurations. As discussed above, uncalendered NMC and LFP (Fig. 1**(A)**) electrodes with low electronic conductivities present a semicircle at the mid-high frequency region (10^6 Hz to 10^2 Hz). The LFP electrode, which has a lower electronic conductivity when compared to the NMC based electrode, shows an even bigger semicircle region and total resistance [6]. On the other hand, the graphite electrode does not show the curved mid-high frequency impedance values, due to its higher intrinsic electronic conductivity. One way of experimentally increasing electronic conductivity by decreasing the contact resistance is to perform electrode calendering. Fig. 1**(B)** illustrates the EI spectra of calendered NMC, LFP and graphite electrodes. Electrode calendering drastically decreases the semicircle region (electronic/contact resistance) and ensures the isolated observation of the impact of ionic resistance on the overall EI spectra. Given that the electronic contribution to the resistance was virtually suppressed due to calendering, the total resistance of the LFP electrode decreased (62.5%) from 0.042 to 0.020 $\Omega.m^2$. A similar change was observed for NMC electrodes after the calendering step (from 0.041 to 0.030 $\Omega.m^2$). In contrast, the overall resistance for the graphite electrode increased after calendering, which is due to an increase in the ionic resistances only, given that the electronic resistances are not a limiting factor for graphite electrodes.

In the following parts of our article, we aim to use our 4D-resolved model to investigate the impact of porosity heterogeneity on the electrodes' electrochemical response. As electrode mesostructures are generated stochastically to control porosity, calendering process impact on the electrode electronic conductivity cannot be explicitly simulated. Therefore, we need to find out the exact value above which the electronic conductivity stops being a limiting source of impedance in the

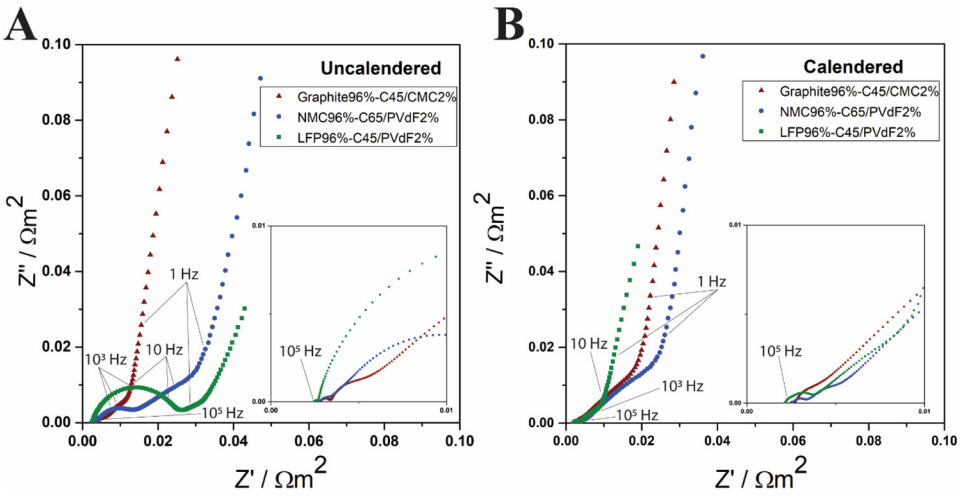

Fig. 1. Experimental Nyquist plots of (A) uncalendered and (B) calendered electrodes in symmetric cells: Graphite 96% - C45/CMC 2% (red), NMC 96% - C65/PVdF 2% (blue) and LFP 96% - C45/PVdF 2% (green).

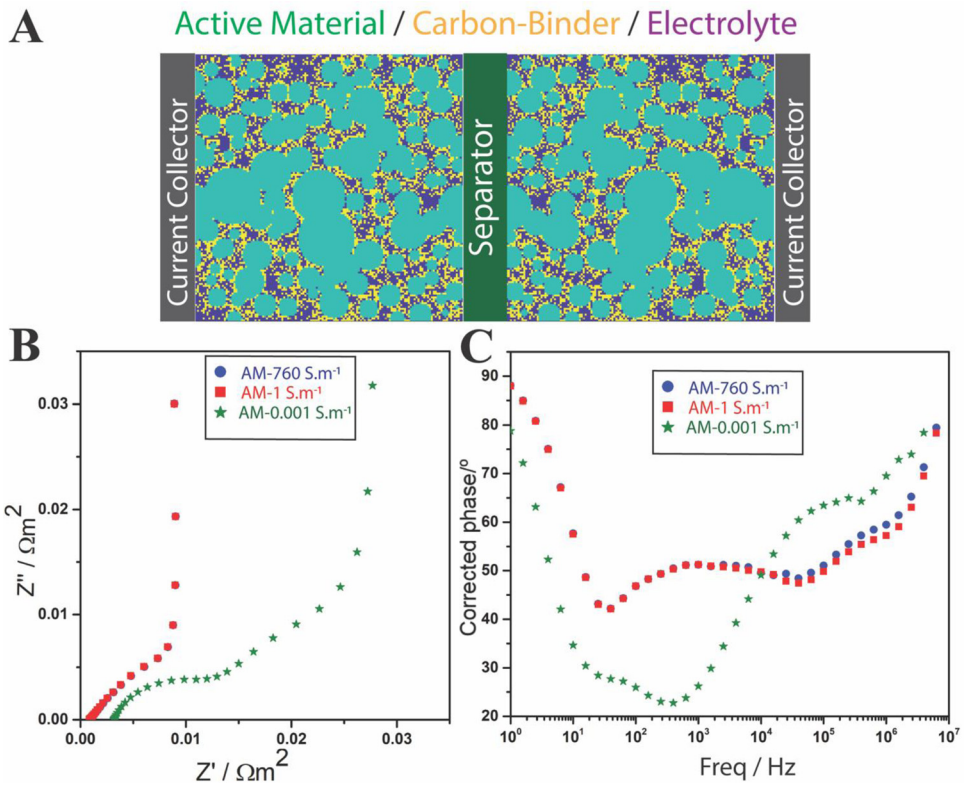

Fig. 2. (A) 2D cut view of the simulated symmetric cell. (B) Simulated Nyquist and (C) Bode plots of NMC 96% - CBD 4%symmetric cells with different electronic conductivities of the NMC active material. The EI spectrum of AM-760 S.m $^{-1}$ (blue) is superposing with AM-1 S.m $^{-1}$ (red).

simulated electrodes. For this purpose, several EIS simulations were carried out by setting different AM electronic conductivity values. Fig. 2**(A)** shows a cut view of the simulated 3D symmetric cell using one of our *in silico*-generated electrode mesostructures. Fig. 2**(B)** and **(C)** show the Nyquist and Bode plots obtained by the simulations. When the electronic conductivity of the AM was set to be of 0.001 S.m $^{-1}$ (as experimentally measured for NMC electrodes), the EIS simulations were consistent with the experimental EIS measuresements (Fig. 1**(A)**) [25]. However, when setting a higher electronic conductivity (1 and 760 S.m $^{-1}$) in the model, the electronic resistance coming from the AM is observed to disappear (semicircle region) and only the ionic resistance (45° slope line) is observed. The simulated EIS spectra with high electronic conductivity values are consistent then with the experimental EIS measurements performed with calendered electrodes (Fig. 1**(B)**). In short, the above analysis shows that by sufficiently increasing the electronic conductivity of the AM, we ensure the dominating presence of the 45° slope line appearing between 10^5 Hz to 10 Hz in Fig. 2**(B)**. This impedance feature corresponds to the electrolyte resistance due to ionic migration limitations in the porous electrode [22]. Additionally, the Bode plot (Fig. 2**(C)**) shows that, for AM conductivities of 1 and 760 S.m $^{-1}$, the corrected phase angles remain between 43° and 50° (10^5 Hz to 10 Hz) as theoretically expected [22].

Consequently, all contact resistances are neglected and bulk electronic conductivity of AM domain was set to 1 S.m $^{-1}$ (higher than in reality) in our simulations as shown in the following sections of our article. These assumptions ensure separating electronic and ionic contributions to the electrode's impedance response and allow us to investigate the impact of the electrode architecture on its ionic resistance.

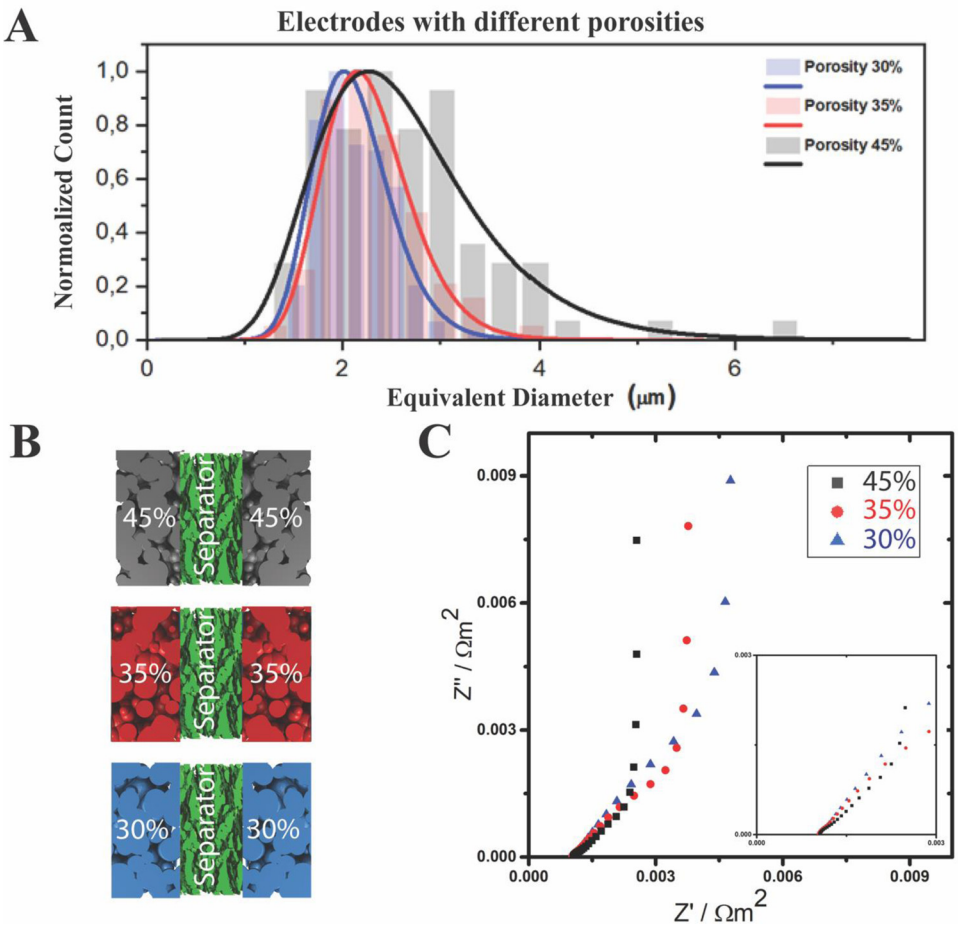

Fig. 3. (A) Normalized pore size distribution of stochastically generated AM 96% - CBD 4% electrodes with porosities 30%, 35% and 45%. (B) Schematics of the simulated electrodes with different porosities in symmetric cells (AM and CBD represented as a merged single solid in grey, red and blue color and pores represented in black color). (C) Simulated Nyquist plots for the three electrode porositues.

3.2. Understanding electrode porosity effects on ionic resistance

Once our 4D-resolved model is correctly calibrated to isolate the ionic resistance contributions, the influences of the electrode porosity on the overall ionic resistance and the tortuosity factors were studied. For this, three electrodes with 30%, 35% and 45% porosities were stochastically generated and simulated by using our model under a virtual symmetric cell configuration. (Fig. 3).

Usually, the PSD of the electrodes changes simultaneously when changing the electrode porosity. Therefore, the PSD of the *in silico*-generated electrodes was assessed to quantify exactly how much pore sizes changed by decreasing the electrode porosity. Fig. 3**(A)** shows that an electrode with 45% porosity has the broadest PSD among the three electrodes with 1.0 μm to 6.0 μm equivalent diameter pores. The smallest standard deviation of PSD was found for the electrode with 30% porosity, as expected. Still, it is clear from the results that the differences in the pore size distributions between different electrodes is slim. These small differences allow us to isolate and systematically study the effect of electrode porosity independently from other geometrical factors. Generated electrodes with different porosities are used in symmetric cell EIS simulations. The Schematics of the electrodes with different porosities used in these simulations are given in Fig. 3**B**.

In the Nyquist plot (Fig. 3**(C)**), the sloping region (mid-to-high frequency) increases when the electrode porosity is reduced from 45% to 30%, ascribing to the higher ionic resistance caused by the low amount of electrolyte and a longer migration path for ions. In addition, the resistance of the electrode increases from 0.0025 to 0.0045 $\Omega.m^2$ when the electrode porosity decreases from 45% to 30%. Furthermore, it is crucial to notice that high porosity electrodes lead to electrical double layer formation at high frequencies faster than the electrodes with lower porosities, which can be explained by an easier path for ions to reach the surface of the solid materials within the electrode.

Fig. 4 shows the ionic impedance of a cross-sectional cut at half of the thickness of the electrode, parallel to the surface at 10^2 Hz. The illustration shows that pores are better connected at higher porosities, which allows easier ionic transport. According to the cross-sectional 2D cut plots (Fig. 4**(A)**), the electrolyte resistance inside the electrode increased when the electrode porosity decreased. Furthermore, higher resistance regions were observed for the CBD domain for the electrode with lower porosity. The explanation of this phenomenon can be found in our recent publications [25,26,30]. Corresponding 3D videos of the simulations are given in SI section.

Table 2 displays the calculated values of ionic resistances (R_{ion}) of the electrolyte within the porous electrodes, the electrode tortuosity factors (τ_{EIS}) calculated through the graphical method proposed by Landesfeind *et al.,* [24] and the tortuosity factors (τ_{factor}) calculated using TauFactor. As expected, the lower the porosity, the higher the ionic resistance and the higher the tortuosity factors (τ_{EIS} and τ_{factor}).

3.3. Designing heterogeneous electrode architectures with improved performance

In the last section we found that highly porous electrodes are beneficial for achieving low ionic resistances which is crucial under high C-rate operation. However, a tradeoff exists between active mass loading and rate capability, which is basically a tradeoff between energy and power densities. Having therefore understood the principles of ionic resistance contributions in EIS, we then envisioned electrode architectures that could optimize rate capabilities, for a fixed average porosity and thickness, by tuning their mesostructural heterogeneities. To do this, the electrodes with different porosities discussed above were virtually

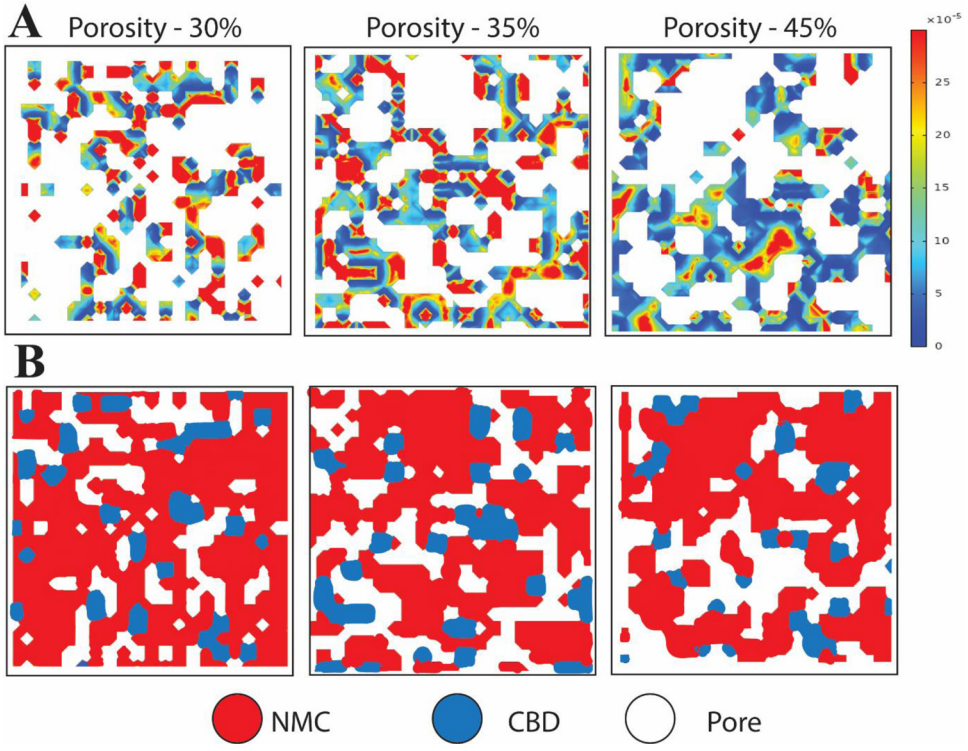

Fig. 4. (A) Simulated NMC 96% - CBD 4% electrode cross-sectional impedance 2D plots at 100 Hz frequency, corresponding to the ionic contribution to the total measured impedance. (B) Scheme of the cross-section cut, where each phase is explicitly tagged with different colors. The cut-views were done at half of the electrode thickness parallel to the current collector surface.

Table 2
Ionic resistances (R_{ion}) of the electrolyte within the electrode pores and tortuosity factors caculated using TauFactor (τ_{factor}) and using the approach proposed by Landersfeind *et al.* (τ_{EIS}) [24].

	Porosity – 30%	Porosity – 35%	Porosity – 45%
Electrode thickness	25 μm	25 μm	25 μm
Tortuosity factor (τ_{factor})	2.15	1.89	1.59
Tortuosity factor (τ_{EIS})	3.3	2.8	1.8
Ionic Resistance $_{(EIS)}$ R_{ion}/Ω m^2	0.011	0.008	0.004

Table 3
Ionic resistances (R_{ion}) of the electrolyte within the electrode pores and tortuosity factors caculated using TauFactor (τ_{factor}) and using the approach proposed by Landersfeind *et al.* (τ_{EIS}) [24].

	Cell-1Sep-45–35–30	Cell-2Sep-30–35–45	Cell-3Sep-35–30–45	Cell-4Sep-45–3035
Electrode thickness	75 μm	75 μm	75 μm	75 μm
Tortuosity factor (τ_{factor})	1.81	1.81	1.81	1.81
Tortuosity factor (τ_{EIS})	1.5	2.8	2.2	1.7
Ionic Resistance $_{(EIS)}$ R_{ion}/Ω m^2	0.013	0.024	0.019	0.015

assembled as one electrode to create heterogeneity of porosity along the electrode thickness (cartesian coordinate Z). Then, the constructed virtual symmetric cells were studied systematically to map the impact of the heterogeneous porosity on the total ionic resistance.

The obtained electrodes are shown schematically in Fig. 5(A). Their corresponding EIS simulation results are shown in Fig. 5(B) and (C), in the form of Nyquist and Bode plots, respectively. The calculated ionic resistance and tortuosity factors for these simulated symmetric cells are given in Table 3. Even though the four studied configurations have the same average porosity, the difference of the ionic resistances between them is significantly different, as it can be seen from the Nyquist plots (Fig. 5(B)).

Cell-1, with the highest porosity (45 %) close to the separator, shows the lowest ionic resistance (0.013 Ω.m^2) with a low tortuosity factor τ_{EIS} of 1.5. In contrast, Cell-2, with the lowest porosity (30 %) close to the separator region, has the highest ionic resistance 0.024 Ω.m^2 and a tortuosity factor τ_{EIS} of around 2.8. According to these results, adjusting the electrode porosity distribution can reduce the ionic resistance by almost 50% while maintaining the overall porosity. When comparing Cell-1 and Cell-4, we demonstrate that having a progressively decreasing porosity from the separator to the current collector can reduce ionic resistance, which results in a drastic improvement of the rate capability of the electrodes for the same areal loading. Additionally, the diffusional tortuosity factors (τ_{factor}), for all four cells were calculated giving a value of around 1.81 (Table 3), which is in striking contrast with the EIS-calculated electrode tortuosity factor (τ_{EIS}) values. These results show that diffusional tortuosity factors are not always adequate when trying to characterize battery electrodes.

In order to validate the predicted simulation trends, single-layer and bi-layer electrodes were prepared by the Bellcore process [32]. The bi-layer electrode consisted of two layers where each layer had a porosity of 40% and 55%. The manufactured single-layer and bi-layer electrodes were put in symmetric cell format for the EIS experiments. Fig. 6**(A)** shows Nyquist plots of the single-layer electrodes with different porosi-

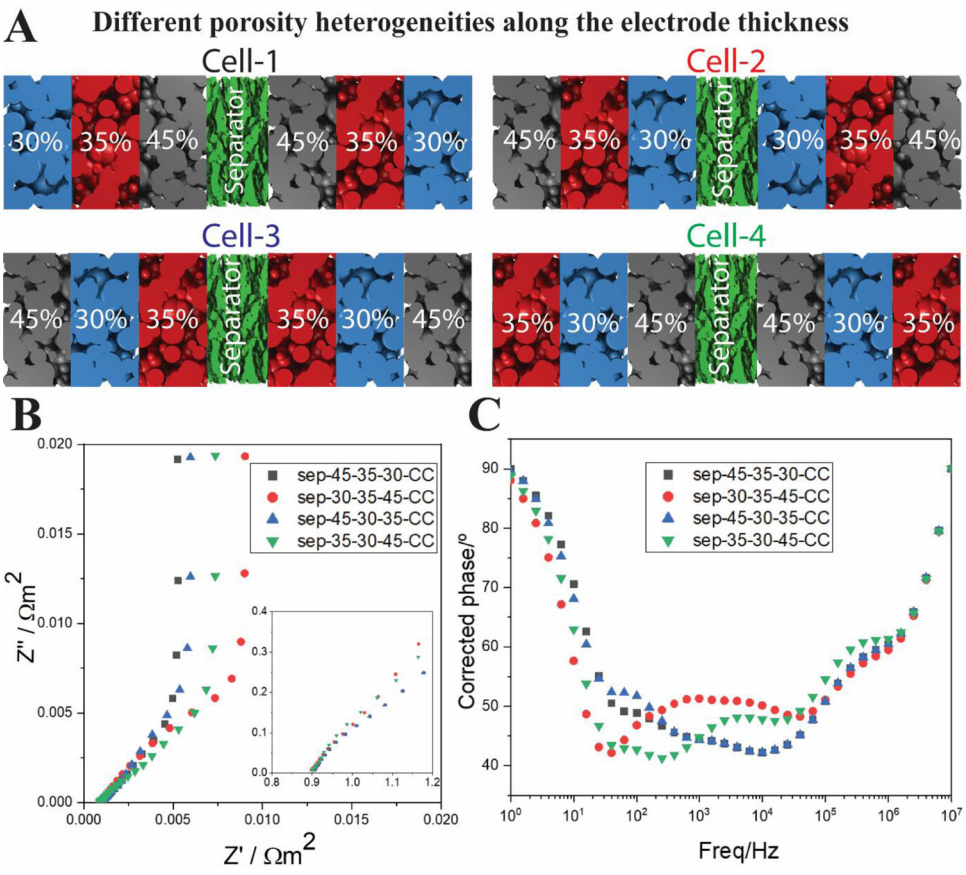

Fig. 5. (A) Schematics of the different simulated symmetric cells with different porosity heterogeneities across the thickness. (B) Simulated Nyquist and (C) Bode plots for these symmetric cells.

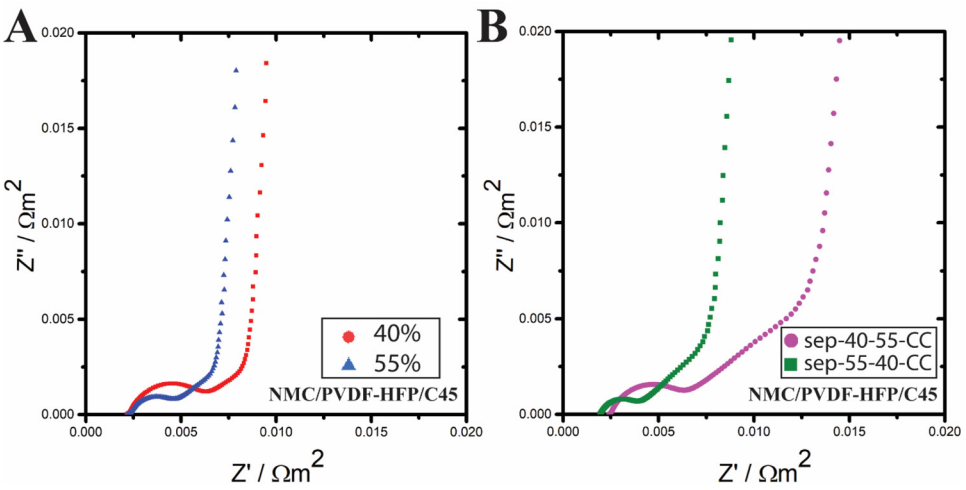

Fig. 6. Nyquist plot of experimental symmetric cells (A) NMC/PVDF-HFP/C45 electrodes with 40% and 55% porosity. (B) NMC/PVDF-HFP/C45 Bi-layer electrodes consisted of two layers across the thickness (from the separator to the current collector side) where each layer had a porosity of 40% and 55% respectively.

ties. Consistently with the simulation results (Fig. 3**(C)**), the electrode with 40% porosity showed higher resistance (0.0085 Ωm^2) than the electrode with 55% porosity (0.0055 Ωm^2). Fig. 6**(B)** shows the Nyquist plot where bi-layer electrodes were assembled to mimic the gradual porosity decreases/increases from the separator to the current collector side. The electrode with the highest porosity (55%) close to the separator shows the lowest ionic resistance 0.007 $\Omega.m^2$ and at the same time, the electrode with the lowest porosity (40%) close to the separator region has the highest ionic resistance 0.014 $\Omega.m^2$. According to the experiments, adjusting the electrode porosity distribution can reduce the ionic resistance by almost 50% while maintaining the overall porosity and the areal loading. This finding is in perfect agreement with the simulation results.

In summary, EIS simulations predicted that the total ionic resistance is strongly correlated with electrode heterogeneity and these predictions were confirmed experimentally. Therefore, when keeping the same overall porosity and areal loading, a desirable electrode mesostructure with a minimized impedance should have a porosity that gradually decreases from separator to current collector. This shows the significant impact of electrode design on electrochemical performance.

Besides the EIS simulations, discharge simulations for the same electrode mesostructures used in the modeling calculations above were carried out based on a half-cell configuration vs. lithium (Fig. 7**(A)**). The simulations carried out at 5C, 3C and 1C rates for all the structures and the results of two electrodes, Halfcell-1 and Halfcell-2, with the most significant difference, are shown in Fig. 7**(B)**. Both of the simulated half-

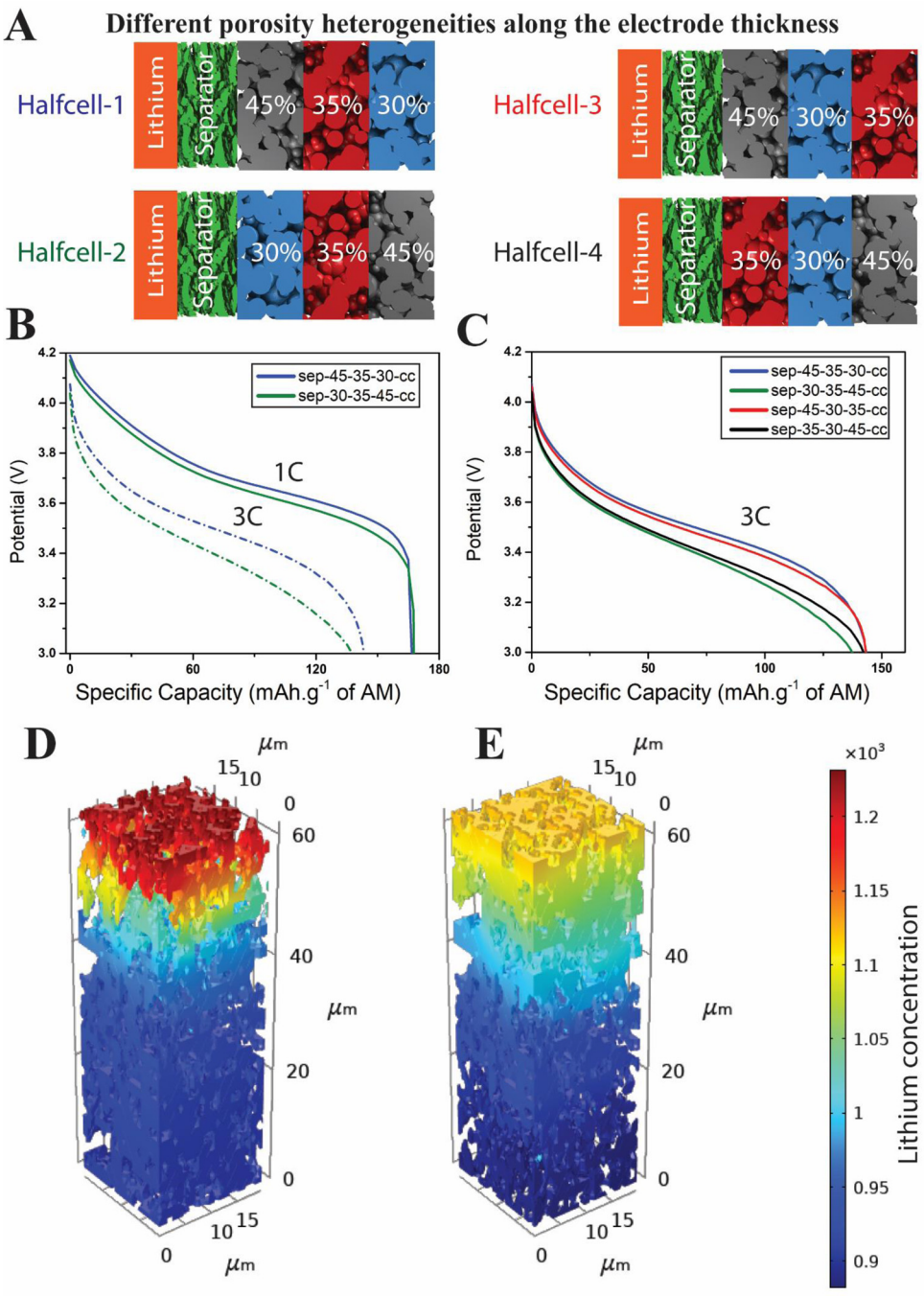

Fig. 7. (A) Schematic of the simulated half cells with different porosity heterogeneities along the thickness (B). Simulated discharge curves for all the half cells for Half-cell-2 and Half-cell-1 at 1C rate and 3C rate (C). Simulated discharge curves for all the half cells at 3C rate. (D) and (E) representation of the lithium concentration in the electrolyte at the end of discharge simulation for Half-cell-2 and Half-cell-1 at 3C rate, respectively (the separator and the current collector are located respectively at the top and bottom of the electrode mesostructures).

cells showed the same capacity (166 mAh g^{-1}) at 1C rate with a small difference in the overall potential between half-cells. However, when simulations were carried under higher C rates (5C and 3C), Half-cell-1, with the electrode with the highest porosity close to the separator, exhibited the highest gravimetric discharge capacity, while Half-cell-2, with the electrode with the lowest porosity close to the separator, delivered the lowest gravimetric capacity among all the electrodes. The results of the discharge simulations at 3C rate for all the cells are given in Fig. 7**(C)**. In agreement with our EIS simulations, discharge simulations showed the same trends for all the corresponding electrodes, where the electrode architecture with progressively decreasing porosity from separator to current collector offers the highest performance.

Fig. 7**(D)** and **(E)** represent the lithium concentration in the electrolyte phase at the end of discharge for Half-cell-2 and Half-cell-1, respectively. In Half-cell-2, the high concentration of lithium close to the separator dramatically decreases along the thickness of the electrode. On the other side, lithium concentration spreads more homogeneously along the thickness of the electrode in Half-cell-1, which has higher porosity close to the separator region. The electrode region with lower electrolyte concentration indicates electrolyte depletion, which can limit utilization of the electrode in that region. The electrolyte depletion will be more serious with increasing electrode thickness and can lead to very low utilization of AM in some regions. In Half-cell-2, the lowest porosity close to the separator reduces the contact surface between NMC and electrolyte - and limits the ion migration along the electrode, which reduces the utilization of the high porosity layer next to the current collector. Also, it is essential to mention that lower porosity near the current collector region ensures better contact between the

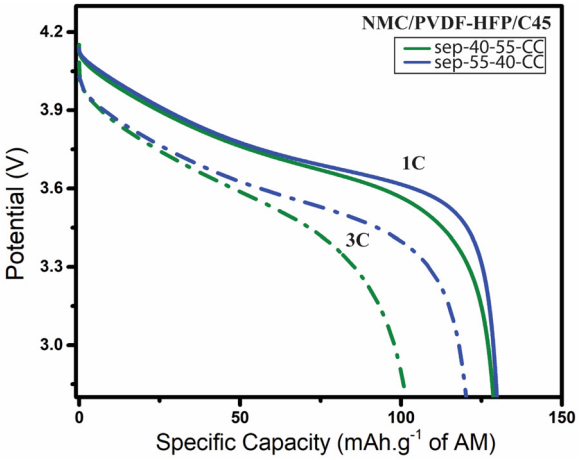

Fig. 8. Experimental discharge curves at 1C and 3C rates for the half-cell format Lithium metal vs NMC/PVDF-HFP/C45 bi-layer electrodes constituted of two layers across the thickness where each layer had a porosity of 40% and 55% respectively.

electrode and the current collector, consequently allowing better electronic fluxes.

On top of the model-based calculations, comparable experiments were performed to reproduce the predictions. Bi-layer electrodes, which mimic the gradual porosity, decrease/increase from the separator to the current collector side, were built in half-cell format against lithium metal to test the rate capability of the electrodes. Coherent with simulations, experiments were tested at 1C and 3C rates. The corresponding discharge curves for the two electrodes are given in Fig. 8. Both electrodes had the same capacity (135 $mAhg^{-1}$) at 1C rate. Still, there is a small difference in overpotential between electrodes as predicted by the simulations. By increasing the C rate from 1 to 3, the difference in capacity diverged between electrodes. Coherent with the simulation results, the electrode with the highest porosity close to the separator exhibited the highest gravimetric discharge capacity, while the electrode with lowest porosity close to the separator delivered the lowest gravimetric capacity among two electrodes. This also agrees with other recent published experimental results where electrodes with high porosity close to separator while maintaining same average porosity demonstrated superior performance at high rates [36,37].

4. Conclusion

In the scope of this work, a 4D (3D in space + time) physical model was successfully used to simulate and analyze the electrode porosity heterogeneity effect on the overall ionic resistance. Furthermore, the modeling results were compared and validated with experimental results. Different electrodes with different mesostructures were generated by using our *in house* INNOV application.

The first part of the study is devoted to mapping the role of ionic and electronic resistances on EIS spectra by comparing experimental NMC, LFP and graphite uncalendered and calendered electrodes. On top of it, simulations with different AM electronic conductivities were carried to eliminate electronic impedance contributions and to assess ionic impedances only.

In the second part of the work, a comparison of electrodes with different porosities was performed based on EIS simulations. As expected, the results show that a lower porosity leads to a higher ionic impedance and electrode tortuosity factor. Tortuosity factors (τ_{EIS}) calculated by the EIS method and tortuosity (τ_{factor}) based on diffusion modeling were compared for all the cases. In agreement with recent literature, we conclude that the EIS-calculated electrode tortuosity factor (τ_{EIS}) in symmetric cells is better suited than the diffusion-based calculated tortuosity factor (τ_{factor}) for battery electrode characterization.

Other electrodes with different porosities were virtually built to study the effect of inhomogeneous porosity across the electrode thickness . Furthermore, virtually generated cells were used in our 4D-resolved model to study EIS in symmetric cell configuration and galvanostatic discharge in half cell setups. The results coming from both simulation and *in house* experiments, showed that electrode heterogeneity along the thickness direction has a significant effect on the ionic impedance and capacity of the electrode. The study showed that the electrode region close to the separator side has the most prominent role in ionic impedance and tortuosity factors which consequently influences the overall capacity. Therefore, to obtain the optimal electrode mesostructure with the highest performance, electrode porosity must be constructed to decrease from the separator side to the current collector side.

Author contribution

Abbos Shodiev: Conceptualization, Methodology, Model development, Formal analysis, Data curation, Investigation, Visualization, Software, Writing – review & editing, Writing – original draft. **Mehdi Chouchane:** Model development, Investigation, Data curation, Review & editing. **Miran Gaberscek:** Conceptualization, Data curation, Investigation, Formal analysis, Writing – review & editing. **Oier Arcelus:** Software, Formal analysis, Visualization, Data curation, Writing – review & editing. **Jiahui Xu**: Investigation, Writing – review & editing. **Hassan Oularbi**: Investigation, Writing – review & editing. **Jia Yu:** Visualization Writing – review & editing. **Jianlin Li:** Investigation, Writing – review & editing. **Mathieu Morcrette:** Investigation, Methodology, Software, Formal analysis, Data curation, Writing – review & editing. **Alejandro A. Franco** Conceptualization, Methodology, Investigation, Writing – review & editing, Supervision, Project administration, Funding acquisition.

Data and code availability

All the data and the codes used in the scope of this work will be publicly available on the ERC-ARTISTIC project's website https://www.erc-artistic.eu

Appendix A. Supplementary data

The supplementary data for this article includes a Supporting Information document and 5 videos showing 3D electrodes under different frequencies for EIS simulations.

Declaration of Competing Interest

The authors declare that they have no known competing financial interests or personal relationships that could have influenced the work reported in this paper.

Acknowledgments

A.A.F., A.S., O.A., J.X., H.O., M.C., and M.M. acknowledge the European Union's Horizon 2020 research and innovation program for the funding support through the European Research Council (grant agreement 772873, "ARTISTIC" project). A.A.F. and O.A. acknowledge partial funding from the Région Hauts de France and from the European Union's Horizon 2020 research and innovation program under grant agreement no 957189 (BIG-MAP). A.A.F. acknowledges the Institut Universitaire de France for the support. J.Y. and A.A.F acknowledge also the funding from the European Union's Horizon 2020 research and innovation programme under grant agreement no 875489 (SONAR).

Supplementary materials

Supplementary material associated with this article can be found, in the online version, at doi:10.1016/j.ensm.2022.01.058.

References

[1] A.A. Franco, A. Rucci, D. Brandell, C. Frayret, M. Gaberscek, P. Jankowski, P. Johansson, Boosting rechargeable batteries R&D by multiscale modeling: myth or reality? Chem. Rev. 119 (2019) 4569–4627 https://doi.org/, doi:10.1021/acs.chemrev.8b00239.

[2] J. Li, Z. Du, R.E. Ruther, S.J. An, L.A. David, K. Hays, M. Wood, N.D. Phillip, Y. Sheng, C. Mao, S. Kalnaus, C. Daniel, D.L. Wood, Toward low-cost, high-energy density, and high-power density lithium-ion batteries, JOM 69 (2017) 1484–1496 https://doi.org/, doi:10.1007/s11837-017-2404-9.

[3] Z. Du, D.L. Wood, C. Daniel, S. Kalnaus, J. Li, Understanding limiting factors in thick electrode performance as applied to high energy density Li-ion batteries, J. Appl. Electrochem. 47 (2017) 405–415 https://doi.org/, doi:10.1007/s10800-017-1047-4.

[4] S. Ahmed, I. Bloom, A.N. Jansen, T. Tanim, E.J. Dufek, A. Pesaran, A. Burnham, R.B. Carlson, F. Dias, K. Hardy, M. Keyser, C. Kreuzer, A. Markel, A. Meintz, C. Michelbacher, M. Mohanpurkar, P.A. Nelson, D.C. Robertson, D. Scoffield, M. Shirk, T. Stephens, R. Vijayagopal, J. Zhang, Enabling fast charging – A battery technology gap assessment, J. Power Sources. 367 (2017) 250–262 https://doi.org/, doi:10.1016/j.jpowsour.2017.06.055.

[5] L.S. Kremer, A. Hoffmann, T. Danner, S. Hein, B. Prifling, D. Westhoff, C. Dreer, A. Latz, V. Schmidt, M. Wohlfahrt-Mehrens, Manufacturing process for improved ultra-thick cathodes in high-energy lithium-ion batteries, Energy Technol. 8 (2020) 1900167 https://doi.org/https://doi.org/, doi:10.1002/ente.201900167.

[6] R. Elango, A. Demortière, V. De Andrade, M. Morcrette, V. Seznec, Thick binder-free electrodes for Li–ion battery fabricated using templating approach and spark plasma sintering reveals high areal capacity, Adv. Energy Mater. 8 (2018) 1703031 https://doi.org/https://doi.org/, doi:10.1002/aenm.201703031.

[7] S. Malifarge, B. Delobel, C. Delacourt, Experimental and modeling analysis of graphite electrodes with various thicknesses and porosities for high-energy-density Li-ion batteries, J. Electrochem. Soc. 165 (2018) A1275–A1287 https://doi.org/, doi:10.1149/2.0301807jes.

[8] W. Kim, D. Jang, H.J. Kim, Understanding electronic and Li-ion transport of LiNi0.5Co0.2Mn0.3O2 electrodes affected by porosity and electrolytes using electrochemical impedance spectroscopy, J. Power Sources. 510 (2021) 230338 https://doi.org/, doi:10.1016/j.jpowsour.2021.230338.

[9] A. Shodiev, M. Duquesnoy, O. Arcelus, M. Chouchane, J. Li, A.A. Franco, Machine learning 3D-resolved prediction of electrolyte infiltration in battery porous electrodes, J. Power Sources. 511 (2021) 230384 https://doi.org/, doi:10.1016/j.jpowsour.2021.230384.

[10] A. Shodiev, E. Primo, O. Arcelus, M. Chouchane, M. Osenberg, A. Hilger, I. Manke, J. Li, A.A. Franco, Insight on electrolyte infiltration of lithium ion battery electrodes by means of a new three-dimensional-resolved lattice Boltzmann model, Energy Storage Mater. 38 (2021) 80–92 https://doi.org/, doi:10.1016/j.ensm.2021.02.029.

[11] K. Pfeifer, S. Arnold, J. Becherer, C. Das, J. Maibach, H. Ehrenberg, S. Dsoke, Can metallic sodium electrodes affect the electrochemistry of sodium-ion batteries? Reactivity issues and perspectives, ChemSusChem 12 (2019) 3312–3319 https://doi.org/https://doi.org/, doi:10.1002/cssc.201901056.

[12] K. Pfeifer, M.F. Greenstein, D. Aurbach, X. Luo, H. Ehrenberg, S. Dsoke, Interaction between electrolytes and Sb2O3-based electrodes in sodium batteries: uncovering the detrimental effects of diglyme, ChemElectroChem 7 (2020) 3487–3495 https://doi.org/https://doi.org/, doi:10.1002/celc.202000894.

[13] C. Meyer, M. Kosfeld, W. Haselrieder, A. Kwade, Process modeling of the electrode calendering of lithium-ion batteries regarding variation of cathode active materials and mass loadings, J. Energy Storage 18 (2018) 371–379 https://doi.org/, doi:10.1016/j.est.2018.05.018.

[14] C.L. Cobb, M. Blanco, Modeling mass and density distribution effects on the performance of co-extruded electrodes for high energy density lithium-ion batteries, J. Power Source. 249 (2014) 357–366 https://doi.org/, doi:10.1016/j.jpowsour.2013.10.084.

[15] W.B. Hawley, J. Li, Electrode manufacturing for lithium-ion batteries—analysis of current and next generation processing, J. Energy Storage 25 (2019) 100862 https://doi.org/, doi:10.1016/j.est.2019.100862.

[16] K.G. Gallagher, S.E. Trask, C. Bauer, T. Woehrle, S.F. Lux, M. Tschech, P. Lamp, B.J. Polzin, S. Ha, B. Long, Q. Wu, W. Lu, D.W. Dees, A.N. Jansen, Optimizing areal capacities through understanding the limitations of lithium-ion electrodes, J. Electrochem. Soc. 163 (2016) A138–A149 https://doi.org/, doi:10.1149/2.0321602jes.

[17] T. Lombardo, M. Duquesnoy, H. El-Bouysidy, F. Årén, A. Gallo-Bueno, P.B. Jørgensen, A. Bhowmik, A. Demortière, E. Ayerbe, F. Alcaide, M. Reynaud, J. Carrasco, A. Grimaud, C. Zhang, T. Vegge, P. Johansson, A.A. Franco, Artificial intelligence applied to battery research: hype or reality? Chem. Rev. (2021) https://doi.org/, doi:10.1021/acs.chemrev.1c00108.

[18] R. Kant, M.B. Singh, Theory of the electrochemical impedance of mesostructured electrodes embedded with heterogeneous micropores, J. Phys. Chem. C. 121 (2017) 7164–7174 https://doi.org/, doi:10.1021/acs.jpcc.7b01287.

[19] M. Chouchane, O. Arcelus, A.A. Franco, Heterogeneous solid-electrolyte interphase in graphite electrodes assessed by 4D-resolved computational simulations, Batter. Supercaps 4 (2021) 1457–1463 https://doi.org/https://doi.org/, doi:10.1002/batt.202100030.

[20] D. Parikh, T. Christensen, J. Li, Correlating the influence of porosity, tortuosity, and mass loading on the energy density of LiNi0.6Mn0.2Co0.2O2 cathodes under extreme fast charging (XFC) conditions, J. Power Sources. 474 (2020) 228601 https://doi.org/, doi:10.1016/j.jpowsour.2020.228601.

[21] N. Ogihara, S. Kawauchi, C. Okuda, Y. Itou, Y. Takeuchi, Y. Ukyo, Theoretical and experimental analysis of porous electrodes for lithium-ion batteries by electrochemical impedance spectroscopy using a symmetric cell, J. Electrochem. Soc. 159 (2012) A1034–A1039 https://doi.org/, doi:10.1149/2.057207jes.

[22] S. Malifarge, B. Delobel, C. Delacourt, Determination of tortuosity using impedance spectra analysis of symmetric cell, J. Electrochem. Soc. 164 (2017) E3329–E3334 https://doi.org/, doi:10.1149/2.0331711jes.

[23] J. Landesfeind, M. Ebner, A. Eldiven, V. Wood, H.A. Gasteiger, Tortuosity of battery electrodes: validation of impedance-derived values and critical comparison with 3D tomography, J. Electrochem. Soc. 165 (2018) A469–A476 https://doi.org/, doi:10.1149/2.0231803jes.

[24] J. Landesfeind, J. Hattendorff, A. Ehrl, W.A. Wall, H.A. Gasteiger, Tortuosity determination of battery electrodes and separators by impedance spectroscopy, J. Electrochem. Soc. 163 (2016) A1373–A1387 https://doi.org/, doi:10.1149/2.1141607jes.

[25] A. Shodiev, E.N. Primo, M. Chouchane, T. Lombardo, A.C. Ngandjong, A. Rucci, A.A. Franco, 4D-resolved physical model for electrochemical impedance spectroscopy of Li(Ni1-x-yMnxCoy)O2-based cathodes in symmetric cells: consequences in tortuosity calculations, J. Power Sources. 454 (2020) 227871 https://doi.org/, doi:10.1016/j.jpowsour.2020.227871.

[26] A.C. Ngandjong, T. Lombardo, E.N. Primo, M. Chouchane, A. Shodiev, O. Arcelus, A.A. Franco, Investigating electrode calendering and its impact on electrochemical performance by means of a new discrete element method model: towards a digital twin of Li-Ion battery manufacturing, J. Power Sources. 485 (2021) 229320 https://doi.org/, doi:10.1016/j.jpowsour.2020.229320.

[27] M. Duquesnoy, T. Lombardo, M. Chouchane, E.N. Primo, A.A. Franco, Data-driven assessment of electrode calendering process by combining experimental results, in silico mesostructures generation and machine learning, J. Power Sources. 480 (2020) 229103 https://doi.org/, doi:10.1016/j.jpowsour.2020.229103.

[28] M. Duquesnoy, T. Lombardo, M. Chouchane, E.N. Primo, A.A. Franco, Accelerating battery manufacturing optimization by combining experiments, in: Silico Electrodes Generation and Machine Learning, 2020, pp. 1–33, doi:10.26434/chemrxiv.12473501. ChemRxivhttps://doi.org/.

[29] M. Chouchane, A.A. Franco, Cover feature: an invitation to engage with computational modeling: user-friendly tool for in silico battery component generation and meshing (Batteries & Supercaps 9/2021), Batter. Supercaps 4 (2021) 1375 –1375. https://doi.org/, doi:10.1002/batt.202100202.

[30] M. Chouchane, A. Rucci, T. Lombardo, A.C. Ngandjong, A.A. Franco, Lithium ion battery electrodes predicted from manufacturing simulations: assessing the impact of the carbon-binder spatial location on the electrochemical performance, J. Power Sources. 444 (2019) 227285 https://doi.org/, doi:10.1016/j.jpowsour.2019.227285.

[31] S.J. Cooper, A. Bertei, P.R. Shearing, J.A. Kilner, N.P. Brandon, TauFactor: an open-source application for calculating tortuosity factors from tomographic data, SoftwareX 5 (2016) 203–210 https://doi.org/, doi:10.1016/j.softx.2016.09.002.

[32] C. Gaya, A.A. Franco, C. Surcin, M. Courty, D. Larcher, Carbon-loaded flexible electrode films for Li-O2 cells: preparation, Porosity, Homogeneity and Electrochemical characterization, ChemRxiv (2020) 1–15.

[33] M. Gaberscek, J. Moskon, B. Erjavec, R. Dominko, J. Jamnik, The importance of interphase contacts in Li ion electrodes: the meaning of the high-frequency impedance arc, Electrochem. Solid-State Lett. 11 (2008) https://doi.org/, doi:10.1149/1.2964220.

[34] J. Moškon, M. Gaberšček, Transmission line models for evaluation of impedance response of insertion battery electrodes and cells, J. Power Sources Adv. 7 (2021) https://doi.org/, doi:10.1016/j.powera.2021.100047.

[35] J. Landesfeind, A. Eldiven, H.A. Gasteiger, Influence of the binder on lithium ion battery electrode tortuosity and performance, J. Electrochem. Soc. 165 (2018) A1122–A1128 https://doi.org/, doi:10.1149/2.0971805jes.

[36] M. Wood, J. Li, Z. Du, C. Daniel, A.R. Dunlop, B.J. Polzin, A.N. Jansen, G.K. Krumdick, D.L. Wood, Impact of secondary particle size and two-layer architectures on the high-rate performance of thick electrodes in lithium-ion battery pouch cells, J. Power Sources. 515 (2021) 230429 https://doi.org/, doi:10.1016/j.jpowsour.2021.230429.

[37] S. Kalnaus, K. Livingston, W.B. Hawley, H. Wang, J. Li, Design and processing for high performance Li ion battery electrodes with double-layer structure, J. Energy Storage. 44 (2021) 103582 https://doi.org/, doi:10.1016/j.est.2021.103582.